Journal of Alloys and Compounds 505 (2010) 560–567

Contents lists available at ScienceDirect

Journal of Alloys and Compounds

journal homepage: www.elsevier.com/locate/jallcom

Impact of Pr–Ni substitution on the electrical and magnetic properties of chemically derived nanosized strontium–barium hexaferrites

Muhammad Javed Iqbal*, Saima Farooq

Surface and Solid State Chemistry Laboratory, Department of Chemistry, Quaid-i-Azam University, Islamabad 45320, Pakistan

ARTICLE INFO

Article history:
Received 30 December 2009
Received in revised form 11 June 2010
Accepted 11 June 2010
Available online 23 June 2010

Keywords:
Nanostructured materials
Electronic properties
Scanning electron microscopy
X-ray diffraction

ABSTRACT

This work is part of our comprehensive study on the synthesis and characterization of $Sr_{0.5}Ba_{0.5-x}Pr_xFe_{12-y}Ni_yO_{19}$ ($0.00 \leq x \geq 0.10$, $0.00 \leq y \geq 1.00$) hexaferrite nanomaterials and, to the best of our knowledge, is the first of its kind in this area of research. The results of the study reveal that this material may have potential applications in the area of magnetic and high-frequency devices, particularly those requiring high electrical resistivity to reduce eddy current losses. Solid state studies using X-ray diffraction show characteristic peaks of the magnetoplumbite structure for these compounds. Electrical and magnetic properties of the co-precipitated ferrites were investigated using state-of-the-art techniques. Values of saturation magnetization and remanence are found to increase in the ranges of 66–78 and 43–48 emu/g, respectively, whereas coercivity is inversely related to Pr–Ni content. AC-magnetic susceptibility investigations show a sharp ferri- to paramagnetic transition in the temperature range of 500–672 K. DC-electrical resistivity shows a maxima for the nominal composition: $Sr_{0.5}Ba_{0.44}Pr_{0.06}Fe_{11.4}Ni_{0.6}O_{19}$. The electrical properties of the synthesized materials are discussed in terms of charge-transport via electron-hopping mechanism between Fe^{3+}/Fe^{2+} ions at the octahedral site.

1. Introduction

M-type hexagonal ferrites ($MFe_{12}O_{19}$, M = Ba, Sr, Ca, Pb) are known for their unique electrical and magnetic properties that lead to their extensive use in modern technological applications [1]. The materials are used in computers, magnetic recording devices, magnetic cards, telecommunications equipment, [2,3] as well as permanent magnets. The magnetoplumbite unit cell ($MFe_{12}O_{19}$) of the hexaferrite system contains two formula units consisting of 10 hexagonally closed-packed oxygen layers stacked along the hexagonal basal plane (*c*-axis). The divalent ion, M^{2+}, is substituted for an oxygen atom in every fifth layer. The Fe^{3+} ions are distributed on five different crystallographic sites: three octahedral (12k, 2a and $4f_2$), one tetrahedral ($4f_1$) and one trigonal bipyramidal site (2b) [4]. In $MFe_{12}O_1$, 8 of the 12 Fe^{3+} ions at 12k, 2a and 2b lattice sites have upward spin (↑), while the remaining 4 ions at $4f_1$ and $4f_2$ sites have downward spin (↓). According to the configuration of Fe^{3+} ions, there are 5 unpaired electrons in the 3d orbital, with each Fe^{3+} ion carrying a magnetic moment of 5 μ_B. According to the spin orientation of the iron ions, the total magnetic moment per formula unit of hexaferrite is: $5\mu_B \times (1[Fe1] + 1[Fe2] - 2[Fe3] - 2[Fe4] + 6[Fe5] = 20\mu_B$ [5].

In general, strontium–barium hexaferrites are known for their high electrical resistivity, magnetization and low dielectric losses. These characteristics are fundamental to restraining eddy current losses for applications operating at high-frequencies [6] and are well suited to radio-frequency circuits, inductors such as wireless communications, mobile phones, cameras, laptops, etc., [7–9], high quality filters, and a range of multilayer chip device applications.

Alteration of electrical resistivity, saturation magnetization, remanence, coercivity, and hyperfine parameters for M-type hexaferrites via cationic substitution has been extensively discussed in the literature [3,4]. Tenaud et al. [10] prepared La–Co substituted strontium hexaferrites and found that the values of saturation magnetization and remanence increased initially by doping with La–Co ions and then decreased with increasing the substitution level. The behavior is attributed to the presence of secondary phases in the material composition. Iqbal and Farooq [3] synthesized Ce–Ni doped strontium–barium hexaferrites and noted that substitution of Ce–Ni ions could enhance saturation and remanence magnetization reducing the coercivity at the same time. Lechevallier et al. [11,12] reported the hyperfine parameters of La–Zn/La–Co and Pr–Co substituted strontium hexaferrites. Litsardakis et al. [13] showed that substitution of Gd–Co ions into barium hexaferrites could be utilized to enhance the magnetization and coercivity.

Rare-earth ions in the hexaferrite lattice are known to have low solubility in aqueous systems. Their stoichiometric incorporation leads to the formation of secondary phases [12] that can potentially

* Corresponding author. Tel.: +92 51 90642143; fax: +92 51 90642241.
E-mail address: mjiqauchem@yahoo.com (M.J. Iqbal).

0925-8388/$ – see front matter © 2010 Elsevier B.V. All rights reserved.
doi:10.1016/j.jallcom.2010.06.073

impair the performance of permanent magnets made out of these materials. Rare-earth ions are known to affect the exchange interactions in the crystal structure leading to enhanced magnetization and electrical resistivity [14]. Recently, high values of coercivity have been reported for Nd–Co substituted barium hexaferrite [15].

This work reports the effect of simultaneous substitution of Pr–Ni ions on the electromagnetic properties of $Sr_{0.5}Ba_{0.5}Fe_{12}O_{19}$ hexaferrites. To the best of our knowledge, co-substitution of $Sr_{0.5}Ba_{0.5}Fe_{12}O_{19}$ hexaferrites with Pr–Ni ions and the influence of such a substitution on the electromagnetic properties of M-type hexaferrites has not been reported so far. The presence of Ni^{2+} ion in ferrites is known to reduce the temperature coefficient of coercivity, increasing the magnetization and the electrical resistivity [16]. The rationale for doping of $Sr_{0.5}Ba_{0.5}Fe_{12}O_{19}$ with Pr–Ni ions was to investigate composition effects on the coercivity, electrical resistivity and overall magnetization. Low substitution ranges of Pr (x = 0.0–0.10) and Ni (y = 0.0–1.0) were chosen to synthesize magntoplumbite phase in as pure form as possible.

2. Experimental

2.1. Synthesis of $Sr_{0.5}Ba_{0.5-x}Pr_xFe_{12-y}Ni_yO_{19}$ hexaferrites

M-type hexaferrites of compositions $Sr_{0.5}Ba_{0.5-x}Pr_xFe_{12-y}Ni_yO_{19}$ (x = 0.00–0.10, y = 0.00–1.00) were synthesized using chemical co-precipitation method [15]. $Fe(NO_3)_3{\cdot}9H_2O$ (98%, Merck), $Sr(NO_3)_2$ (≥99%, Aldrich), $Ba(NO_3)_2$ (>99%, Aldrich), $Ni(CH_3COO)_2{\cdot}4H_2O$ (99%, Merck), $Pr(NO_3)_3{\cdot}5H_2O$ (>99%, Aldrich) and NH_4OH (33%, Aldrich) were used as the starting materials. Aqueous solutions of metal ions were prepared with stoichiometric compositions $Sr_{0.5}Ba_{0.5-x}Pr_xFe_{12-y}Ni_yO_{19}$ and then mixed together. Ammonium hydroxide solution (3 M) was used for precipitation of solutions at pH 9. The mixture was stirred for 3 h followed by overnight aging. The collected precipitates comprising of hydroxides of metal ions, ammonium nitrates and water contents [17], were dried in oven at 473 K. The dried product (mainly ammonium nitrates and hydroxides of metal ions) was annealed at 1323 K for 6 h in a temperature-programmed tube furnace, at a heating rate of 5 K min^{-1}. The proposed chemistry of co-precipitation is as follows:

$$x\mathrm{Sr(NO_3)_2\,(aq)}+y\mathrm{Ba(NO_3)_2(aq)}+z\mathrm{Fe(NO_3)_2(aq)}+\mathrm{NH_4OH}\xrightarrow{\mathrm{pH=9}}\underset{\mathrm{Me^{s+}=Sr^{2+},Ba^{2+},Fe^{3+}}}{[\mathrm{Me^{s+}\cdot OH^-}]_m\cdot n\mathrm{H_2O}}$$

$$+w\mathrm{NH_4NO_3}\xrightarrow[\text{drying 473 K}]{}\underset{\text{precursor}}{[\mathrm{Me^{2+}(OH^-)}_m]}+w\mathrm{NH_4NO_3}\xrightarrow[\text{annealing 1323 K}]{}\underset{\text{crystalline}}{\mathrm{Sr_{0.5}Ba_{0.5}Fe_{12}O_{19}}}$$

2.2. Characterization

Precursor sample was analyzed thermo-gravimetrically using a Mettler-Toledo system (TGA/SDTA 851e). The solid phase investigations of synthesized samples were done using X-ray diffractometer (JEOL JDX-60PX), equipped with CuK_α as the radiation source. The diffraction pattern was recorded for 2θ from 20° to 80° with scan step size of 0.02°. The voltage and current of the generator were set at 40 kV and 30 mA, respectively. Quantitative elemental analysis was carried out via energy dispersive X-ray fluorescence (ED-XRF) spectroscopy using a Horiba, MESA-500 spectrometer. Morphological studies of samples were done using a scanning electron microscope (S-3400 SEM). Vibrating sample magnetometer was used at the maximum applied field of 10 kOe, for measuring magnetic properties at room temperature. AC-magnetic susceptibility measurements were made using a laboratory assembled double-coil setup operating at 273 Hz with a magnetic field of 0.1 Oe in the temperature range of 300–703 K [18]. The susceptibility apparatus was calibrated using pure nickel as standard. Disc-shaped pellets were prepared by compressing the powdered sample at 50 kN m^{-2} using hydraulic press (Paul-Weber PW-30). The pellets were used for DC-electrical resistivity and AC-magnetic susceptibility measurements. The resistivity (ρ) was measured in the temperature range of 373–673 K using a two-point probe technique [19].

3. Results and discussion

3.1. Thermal analysis

Fig. 1 shows the TG plots for as-synthesized samples of the strontium–barium hexaferrite with composition ranges in x = 0.00, 0.02 and y = 0.00, 0.20. Dehydration, decomposition and sintering are the most common processes known to occur during heat-treatment of most samples. It can be seen from Fig. 1 that the addition of dopants slightly influenced the thermal behavior of the strontium–barium hexaferrite samples. The TG curves show three distinct steps of weight loss. The first step below 500 K marks the dehydration of the adsorbed water. The second step, between 500 and 550 K, shows the decomposition of metallic hydroxides. In this temperature range, the NH_4NO_3 may also have decomposed to liberate NO_x and O_2 as proposed below [20]:

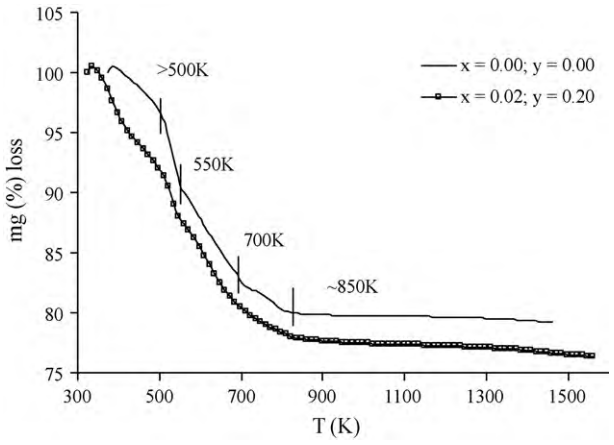

Fig. 1. TG-DTG of as-synthesized samples of (a) $Sr_{0.5}Ba_{0.5}Fe_{12}O_{19}$ and (b) $Sr_{0.5}Ba_{0.48}Pr_{0.02}Fe_{11.8}Ni_{0.2}O_{19}$.

$$\mathrm{NH_4NO_3}\rightarrow\ \mathrm{NO}_x+\mathrm{O_2}+\mathrm{H_2O} \quad (1)$$

The weight loss in the temperature range of 700–900 K is attributed to the formation of an intermediate hematite (α-Fe_2O_3) and monoferrite (MFe_2O_4) phases [21]. The TG plot of the doped sample is akin to the undoped sample, except that a gradual decrease with higher weight loss is observed than that noted in case of undoped sample. This is likely due to additional mass of NH_4NO_3 in the doped precursor.

The TG curves show no noticeable weight loss above 1000 K, most likely due to the onset of M-type hexaferrite phase. The complex structure of the hexaferrite material [22] leads to the suggestion that formation of pure strontium–barium hexaferrite would likely require high annealing temperatures for the elimination of an intermediate (Fe_2O_3) phase.

3.2. Structural analysis

The XRD patterns of the synthesized hexaferrite materials are presented in Fig. 2. XRD analysis reveals that all observed diffraction peaks and Miller indices (hkl) match well with the known pattern of M-type strontium–barium hexaferrite (Fig. 2g) with no extra peaks. This also shows that the crystallization of samples in the single-phase magnetoplumbite structure occurred to very high degree of perfection, with no evidence of impurity and crystal deformation. The crystallite size (D) is calculated by the Scherrer formula:

$$D=\frac{k\lambda}{\beta\cos\theta}, \quad (2)$$

where λ is the X-ray wavelength and is equal to 1.54 Å, β is the half-peak width, θ is the Bragg angle and k is the shape factor that is equal to 0.89 for the hexagonal system. The average crystallite size is found to be in the range of 18–36 nm for the synthesized samples (Table 1), which is much smaller than the value of 5 μm reported for a composition of $Sr_{0.5}Ba_{0.5}Fe_{12}O_{19}$, synthesized by the ceramic method [23]. Lattice constants, a and c, are calculated by

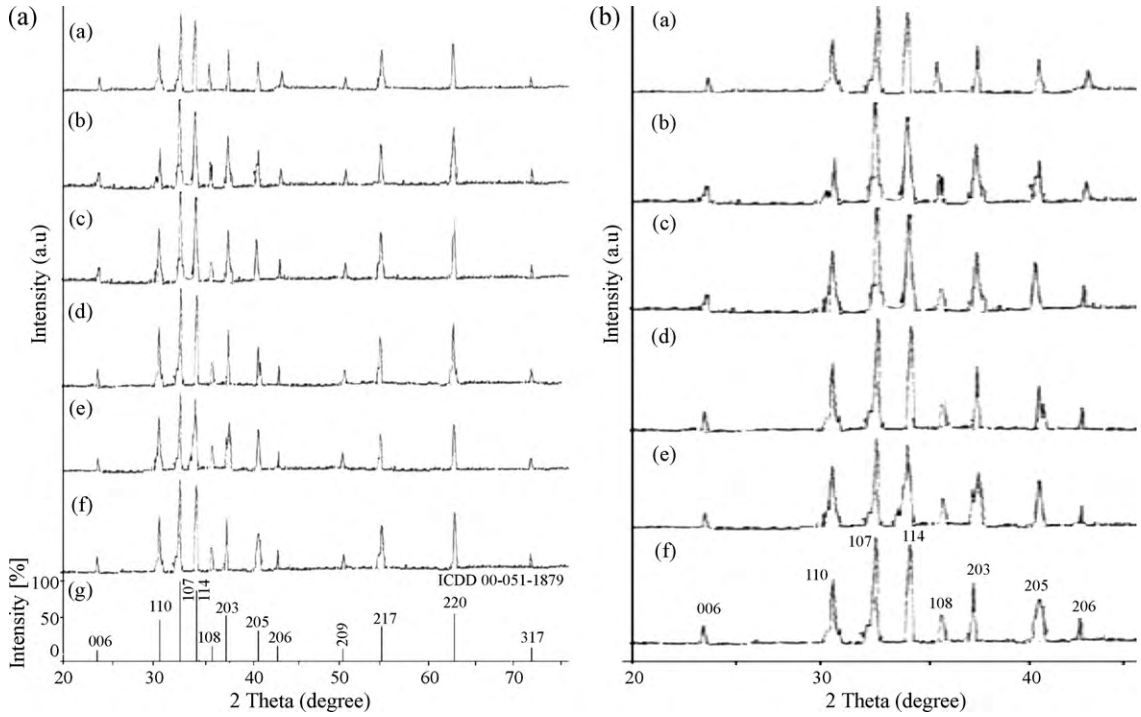

Fig. 2. (a and b) XRD patterns (a) $x = 0.00$, $y = 0.00$; (b) $x = 0.02$, $y = 0.20$; (c) $x = 0.04$, $y = 0.40$; (d) $x = 0.06$, $y = 0.60$; (e) $x = 0.08$, $y = 0.80$; (f) $x = 0.10$, $y = 1.00$ and (g) standard pattern of $Ba_{0.5}Sr_{0.5}Fe_{12}O_{19}$, of Sr–Ba hexaferrite samples with different Pr–Ni contents, and (b) expanded view of samples (a) $x = 0.00$, $y = 0.00$; (b) $x = 0.02$, $y = 0.20$; (c) $x = 0.04$, $y = 0.40$; (d) $x = 0.06$, $y = 0.60$; (e) $x = 0.08$, $y = 0.80$; and (f) $x = 0.10$, $y = 1.00$.

the following equation:

$$\frac{1}{d_{jkl}^2} = \frac{4}{3}\left[\frac{h^2 + hk + k^2}{a^2} + \frac{l^2}{c^2}\right], \tag{3}$$

where d_{hkl} is an inter-atomic spacing. Unit cell volume (V_{cell}) of the hexagonal system is calculated as follows:

$$V_{cell} = 0.866a^2c, \tag{4}$$

where numeric factor is constant for the hexagonal system. The measured density (d_m) is calculated by the mass and volume ($V = \pi r^2 h$) of the sample pellet using the following relation:

$$d_m = \frac{m}{\pi r^2 h} \tag{5}$$

It can be seen that the lattice parameter a, remains nearly constant while the value of c slightly decreases with the increasing substitution of Pr–Ni (Table 1). It also supports the proposition that dopants simply replaced the Ba^{2+}–Fe^{3+} ions without distortion of the hexagonal symmetry of the host strontium–barium hexaferrite. Slight shrinkage in the unit cell volume is observed with Pr–Ni substitution (Table 1), which is interpreted in terms of the substitution of Pr, one of the rare-earth elements that are known for their ability to form strong lanthanide–oxygen bonds. The binding energy of the lanthanide–oxygen octahedra (RO_6) in rare-earth substituted oxide materials is known to be much higher than the transition-metal ion-oxygen octahedra (MO_6), a likely factor in the shrinkage of the crystal lattice in this case [24,25].

The density is seen to decrease with the substitution of Pr–Ni, as shown in Table 1. It appears that the doped elements contribute to the retardation of the process of densification of the hexaferrite matrix. Since doping of lanthanide ions is known to contribute to the stability to the crystal lattice [26]. A similar effect in this case can be seen where an observed diminished grain-growth may be related to the process of nucleation or agglomeration. The observed elemental composition of the synthesized samples matches well with the expected stoichiometry, as indicated by the ED-XRF analysis (Table 2). The results indicate that Pr and Ni entered the hexaferrite lattice, resulting in a single M-type hexagonal phase. This is substantiated by XRD findings shown in Fig. 2. The surface micrographs of the three representative samples $Sr_{0.5}Ba_{0.5}Fe_{12}O_{19}$, $Sr_{0.5}Ba_{0.44}Pr_{0.04}Fe_{11.6}Ni_{0.4}O_{19}$ and $Sr_{0.5}Ba_{0.42}Pr_{0.08}Fe_{11.2}Ni_{0.8}O_{19}$ are shown in Fig. 3(a–c). The surface of the undoped $Sr_{0.5}Ba_{0.5}Fe_{12}O_{19}$ sample (Fig. 3a) appears to be dense with large agglomerated particles. The surface of the samples

Table 1
Crystallite size (D), lattice constants (a, c), unit cell volume (V_{cell}), measured density (d_m), Curie temperature (T_C), DC-electrical resistivity (ρ) at 423 K and activation energy of hopping (E_a) for $Sr_{0.5}Ba_{1-x}Pr_xFe_{12-y}Ni_yO_{19}$ with different Pr_xNi_y contents ($x = 0.00$–0.10, $y = 0.00$–1.00).

Parameters	$x = 0.00$ $y = 0.00$	$x = 0.02$ $y = 0.20$	$x = 0.04$ $y = 0.40$	$x = 0.06$ $y = 0.60$	$x = 0.08$ $y = 0.80$	$x = 0.10$ $y = 1.00$
D (nm) (±0.65)	36	41	32	26	21	18
a (±0.002 Å)	5.880	5.883	5.883	5.884	5.884	5.885
c (±0.017 Å)	23.149	23.150	23.142	23.132	23.123	23.105
V_{cell} (±0.3 Å^3)	693	694	693	694	693	693
d_m (±0.07 g cm^{-3})	3.58	3.41	3.48	3.54	3.57	3.59
Tc (±5 K)	672	652	620	595	580	558
ρ (10^{10} Ω cm at 423 K)	0.502	1.086	1.691	2.255	0.957	0.266
E_a (±0.02 eV)	0.64	0.66	0.67	0.69	0.68	0.66
H_c (kOe)	2.85	2.79	2.52	2.57	2.64	2.70

Table 2
Elemental compositions of $Sr_{0.5}Ba_{1-x}Pr_xFe_{12-y}Ni_yO_{19}$ ($x = 0.00–0.100$, $y = 0.00–1.00$) with different Pr_xNi_y contents as determined by ED-XRF analysis.

Sample compositions	Elements (moles)				
	Sr	Ba	Pr	Fe	Ni
$Sr_{0.5}Ba_{0.5}Fe_{12}O_{19}$	0.500	0.497	–	12.00	–
$Sr_{0.5}Ba_{0.48}Pr_{0.02}Fe_{11.8}Ni_{0.2}O_{19}$	0.498	0.479	0.019	11.80	0.21
$Sr_{0.5}Ba_{0.46}Pr_{0.04}Fe_{11.6}Ni_{0.4}O_{19}$	0.498	0.458	0.039	11.61	0.40
$Sr_{0.5}Ba_{0.44}Pr_{0.06}Fe_{11.4}Ni_{0.6}O_{19}$	0.499	0.439	0.058	11.42	0.60
$Sr_{0.5}Ba_{0.42}Pr_{0.08}Fe_{11.2}Ni_{0.8}O_{19}$	0.500	0.418	0.079	11.20	0.81
$Sr_{0.5}Ba_{0.40}Pr_{0.10}Fe_{11.0}Ni_{1.0}O_{19}$	0.499	0.389	0.097	11.01	1.01

shown in Fig. 3b and c, exhibit a relatively well-defined mixture of individual nanoparticles of well crystalline nature and small aggregates formed as a result of an agglomeration of these individual nanoparticles. The size of these agglomerated particles gets smaller as the dopant content increases, as shown in Fig. 3c. The average particle size calculated from SEM micrographs is in range of 28–57 nm, which are comparable to the crystallite sizes of samples as calculated by Scherrer formula (Table 1).

3.3. Magnetic properties

3.3.1. Magnetization measurements

The hysteresis loops for the substituted Sr–Ba M samples, shown in Fig. 4, represent a sharp increase in magnetization at low applied field that slows down at the high fields. The variation of magnetic parameters: saturation magnetization (M_s), remanence magnetization (M_r) and coercivity (H_c) with Pr–Ni substitutions are shown in Fig. 5 and Table 1, respectively. Fig. 5 shows increase in the values of both M_s and M_r with the substitution of Pr–Ni ions up to $x = 0.06$ and $y = 0.60$. This is likely due to the site occupancy of the doped metal ions at different lattice sites. In M-type hexaferrite, Fe^{3+} ions are distributed on 12k, 2a, 2b lattice sites with an upward spin moment and with downward spins on the $4f_1$ and $4f_2$ lattice sites, as shown in Fig. 6. Four of the upward spins cancel out the four downward spins, and the net magnetic moment is due to the remaining four ferric ions with upward spins. Therefore, each M-type hexaferrite carries the total magnetic moment of 20 μ_B per unit cell [23]. Generally, the magnetic behavior of the ferrimagnetic hexaferrite material is largely governed by the distribution of iron ions on the crystallographic lattice sites and hence the Fe^{3+}–Fe^{3+} exchange interactions (the spin coupling of the 3d electrons). The magnetization of the hexaferrite material varies with the factors influencing the strength of these exchange interactions. In the rare-earth substituted ferrite materials, RE^{3+}–Fe^{3+} interactions also exist via 4f–3d couplings which can cause changes in magnetic properties. The RE^{3+}–RE^{3+} interactions are very weak because they result from indirect 4f–5d–4f coupling [27].

Substitution of the Fe^{3+} ions in the spin-up states (12k, 2a, 2b) appears to cause reduction in magnetization while the substitution in the spin-down ($4f_1$, $4f_2$) states [23] may lead to an increase in the net magnetization. It is reported that the Ni^{2+} ion has a special preference for the $4f_2$ (octahedral) site but may also occupy the 12k site for a higher substitution level (~0.5) [5]. The low level of the doped Ni ions is expected to replace the iron ions from the sites having spins in the downward direction ($4f_2$). The net increase in upward spin is, therefore, expected to increase the total magnetic moment and hence the magnetization. Pr^{3+} ions are located in the Ba^{2+} site, whose nearest neighbor is the 2b lattice site because it is known that the nearest neighbors of Ba^{2+} in the Ba-layer are 12k, $4f_2$ and 2b, where the 2b site is closer to the Ba^{2+} site at a distance of 0.340 nm as compared to the $4f_2$ site which is at a distance of d = 0.366 nm [11]. The substitution of Pr^{3+} to the Ba^{2+} ion induces a perturbation in both electron-density and symmetry around the 2b lattice site, that could strengthen the exchange interactions and hence the magnetization. This is also reported by Ounnunkad [28] for the rare-earth substituted Ba hexaferrite.

The abrupt fall in the values of M_s and M_r for the samples with $x \geq 0.08$, $y \geq 0.80$ appears mainly due to the replacement of Fe^{3+} in the spin-up state (12k) by the doped Ni^{2+} with a low magnetic moment (2 μ_B). This appears to weaken the strength of the exchange interactions resulting in a decreased net magnetization. In addition, the presence of Pr^{3+} ion with low magnetic moment (3.58 μ_B) in the vicinity of Fe^{3+} (5 μ_B) ion would dilute the strength of the exchange interactions to result in the reduction of the total magnetization.

The coercivity, H_c, which is a measure of the strength of the magnetic field required for overcoming the anisotropy to flip over the aligned magnetic moments, is also affected with the dopant substitution (x, y), as shown in Table 1. High value of coercivity (2.85 kOe) is observed for the undoped sample, which is ascribed to the uniaxial magneto-crystalline anisotropy of hexaferrite material along an easy axis (c-axis) [23]. A significant fall in the coercivity is observed with the addition of Pr–Ni contents up to $x = 0.06$, $y = 0.60$ (Table 1). It has been reported that in the M-type hexaferrite, $4f_2$ and 2b sites contribute to their large magneto-crystalline anisotropy [29]. Substitution of the Ni^{2+} at the $4f_2$ site (as Ni^{2+} replaces iron at the $4f_2$ for a low substitution level <0.5) [5] and the perturbation at the 2b lattice site, caused by doping of Pr^{3+} ions, are jointly responsible for the observed decrease in the coercivity (Table 1). Another plausible reason for the observed decrease is that the ionic radius of the dopant Ni^{2+} (0.69 Å) is larger than that of the Fe^{3+} (0.64 Å) so that the uniaxial anisotropy does not remain planar along the easy c-axis. Also, similar behavior has been observed for the Co–Ru doped $Sr_{0.5}Ba_{0.5}Fe_{12}O_{19}$. [23].

An exceptionally high value of coercivity is observed when $x \geq 0.08$, $y \geq 0.80$ (Table 1). Because Ni^{2+} ions substitute for the Fe^{3+} ions at the 12k site for the higher substitution level >0.5 (as mentioned above), as this lattice site does not contribute to magneto-crystalline anisotropy [4], coercivity is expected to enhance. The magnetic anisotropy is the result of accumulative contributions of the magnetic cations in the crystal structure (nickel, iron and praseodymium). Mainly, Ni^{2+} ions are octahedrally coordinated [30], and an increase in their number would increase the single magnetic ion anisotropy to result in the enhancement of the coercivity. Since the spin-orbital coupling is usually much stronger in the rare-earth ions, the substitution of Pr at higher dopant level ($x \geq 0.08$) would also contribute for enhancing the value of coercivity. Similar effects on magnetic properties of the rare-earth doped Mg–Ti ferrites are also reported by other authors [31]. Increase in the magnetization of the synthesized hexaferrites together with the decrease in the coercivity of the Pr–Ni ions doped hexaferrites validates their possible use in magnetic data storage devices.

3.3.2. AC-magnetic susceptibility measurements

Magnetic susceptibility is a parameter of prime significance in the characterization of the magnetic properties of a material. The magnitude of the susceptibility and its temperature dependence provides a significant insight into the magnetic

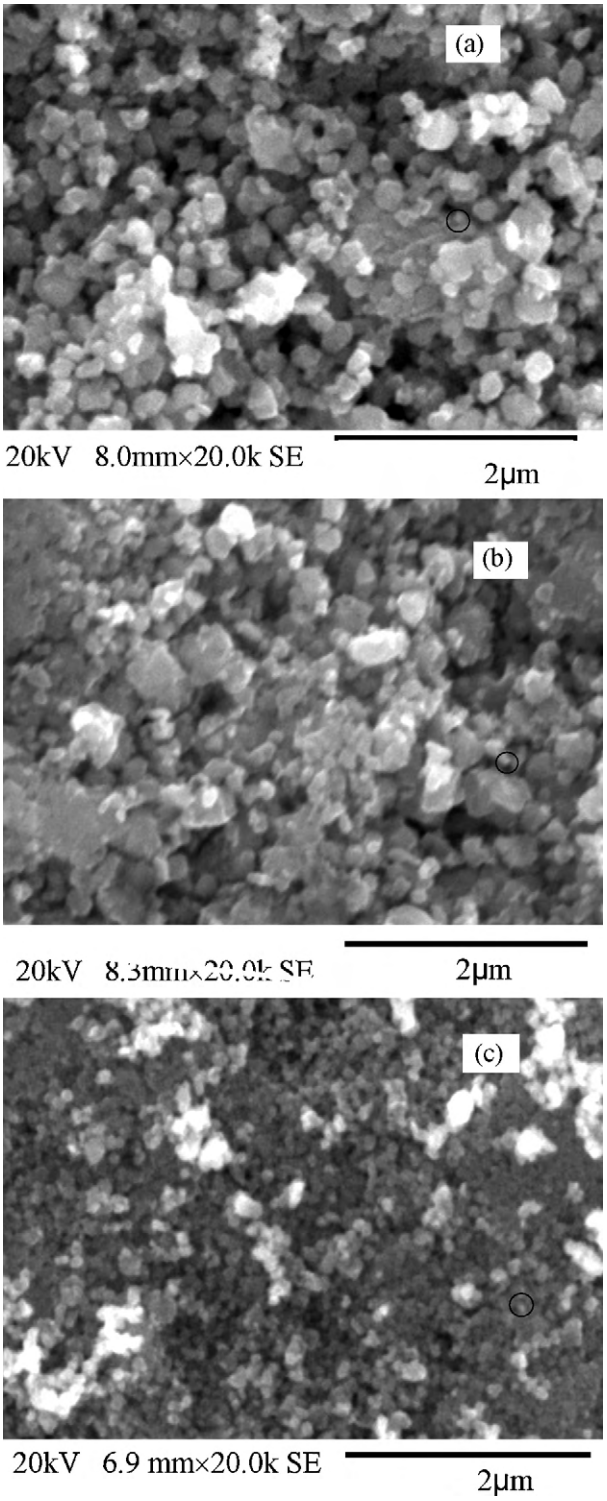

Fig. 3. SEM images of (a) $Sr_{0.5}Ba_{0.5}Fe_{12}O_{19}$, (b) $Sr_{0.5}Ba_{0.46}Pr_{0.04}Fe_{11.6}Ni_{0.40}O_{19}$ and (c) $Sr_{0.5}Ba_{0.42}Pr_{0.08}Fe_{11.2}Ni_{0.8}O_{19}$ samples.

behavior of the materials. The temperature dependence of AC-magnetic susceptibility (χ) is employed in the temperature range of 300–680 K, to characterize the magnetic properties of $Sr_{0.5}Ba_{0.5-x}Pr_xFe_{12-y}Ni_yO_{19}$ ferrite nanoparticles (Fig. 7). The inverse susceptibility ($1/\chi$) decreases with a rise in temperature, then increases sharply after a transition point, where ferrite nanoparticles appear to switch from ferrimagnetic to the paramagnetic state. An ordered arrangement of magnetic moments

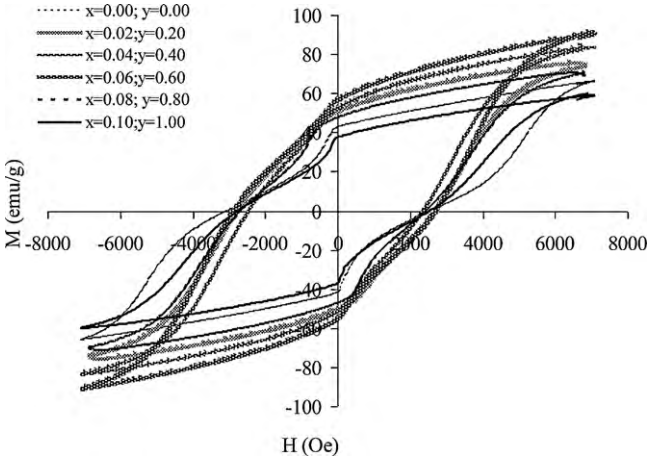

Fig. 4. Hysteresis loops for Sr–Ba hexaferrite samples with different Pr–Ni substitution contents ($x = 0.00–0.100$, $y = 0.00–1.00$).

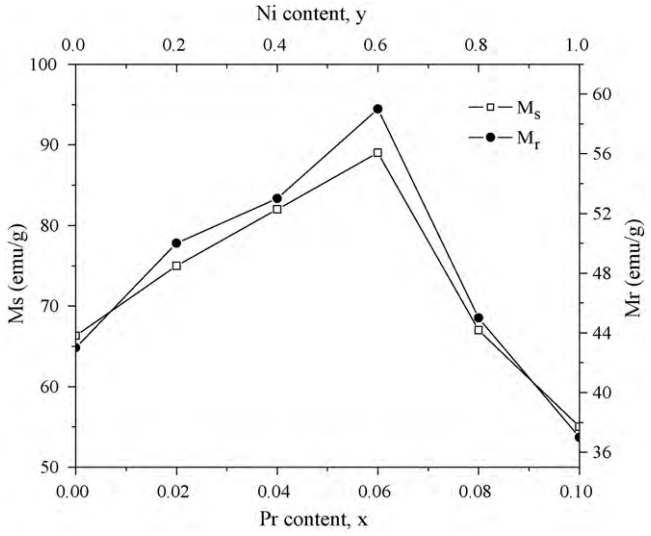

Fig. 5. Effect of Pr–Ni contents on saturation magnetization (M_s) and remanent magnetization (M_r) for Sr–Ba hexaferrite samples containing different Pr–Ni contents.

in the ferrite composition appears to get randomized with a rise in temperature, due to the thermal fluctuations of the individual moments [22]. Beyond the transition temperature termed as Curie temperature (T_C), the material becomes disordered and loses its net magnetization. The sudden increase in $1/\chi$ above T_C confirms the conclusion that a single magnetoplumbite phase structure is formed in all the samples [32] as already predicted by XRD studies (Fig. 2). The linear portion of ($1/\chi$) versus T is extrapolated to the temperature axis to estimate the T_C for all the synthesized samples. The Curie temperature decreases with the addition of the Pr–Ni ions (Table 1), which can be interpreted in terms of the strength of the

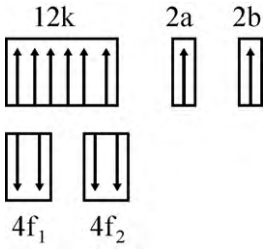

Fig. 6. Spin orientation of Fe^{3+} ions at each crystallographic site.

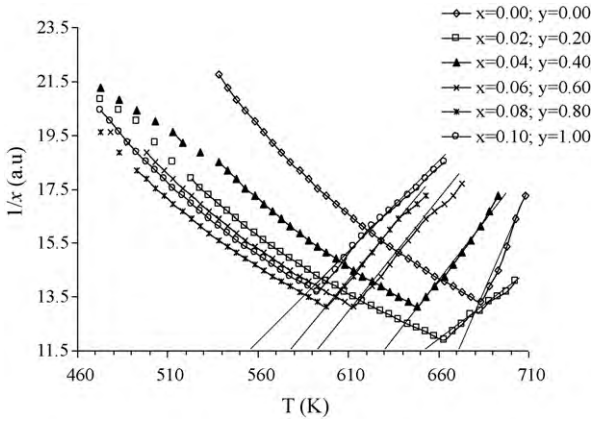

Fig. 7. Plots of AC-magnetic susceptibility of strontium–barium hexaferrite samples containing different Pr–Ni contents ($x = 0.00–0.100$, $y = 0.00–1.00$).

exchange interactions. Such strength is a function of the Fe–O–Fe linkages, which in turn depends upon the number of the Fe ions in the formula unit and their distribution among the lattice sites. Since the magnetic moment of the Pr^{3+} ions is lower than that of the Fe^{3+}, substitution of Pr^{3+} weakens the Fe^{3+}–Fe^{3+}, Fe^{3+}–RE^{3+} exchange interactions. In addition, magnetic moment of the Ni^{2+} ($2\,\mu_B$) is also lower than that of the Fe^{3+} ($5\,\mu_B$). Therefore, substitution of the Pr–Ni ions at or near the crystallographic sites of the Fe weakens the strength of the net exchange interactions and hence decreases the value of T_C. Similar findings for the doped ferrite materials are also reported by other authors [30,33].

3.4. Electrical properties

Electrical resistivity is an important parameter of the ferrites from applications point of view. The DC-electrical resistance (R) is measured in the temperature range of 300–673 K by the two-point probe method [19] and then used for the calculation of resistivity (ρ) using the following relation:

$$\rho = R\frac{A}{h}, \tag{6}$$

where R is the resistance, h is height and A ($A = \pi r^2$) of the pellet (of the dimensions as mentioned above) of sample having radius r.

Fig. 8a shows DC-electrical resistivity as a function of temperature in the range, 300–673 K. The value of resistivity initially increases as the temperature reaches the so-called metal–semiconductor transition temperature, during which the material shows metal-like behavior. It is followed by a decrease in resistivity that is typical of semiconductors in general. The metal-like behavior is observed for all samples in the temperature range, 343–363 K. This is attributed to the presence of a minor amount of moisture left over in situ, and absorbed at the surface of the sample due to the porous nature of the samples [4]. The compositional dependence of the DC-resistivity (ρ) at 423 K is presented in Table 1. It is seen that the value of resistivity increases up to a substitution level of $x = 0.06$, $y = 0.60$. The conduction in ferrites is interpreted in terms of Verwey [34] mechanism that proposes the electronic exchange between ions of the same element with more than one valance state and distributed among the octahedral sites in the crystal lattice. In addition, the conduction in these ferrites is attributed to the hopping of electrons from Fe^{3+} to Fe^{2+} ions [35]. The magnitude of this electron exchange would normally depend upon the number of Fe^{2+}/Fe^{3+} ion pairs present at the octahedral site. Furthermore, a proximity of iron ions at the octahedral site also supports the probability of hopping mechanism for electrical conduction.

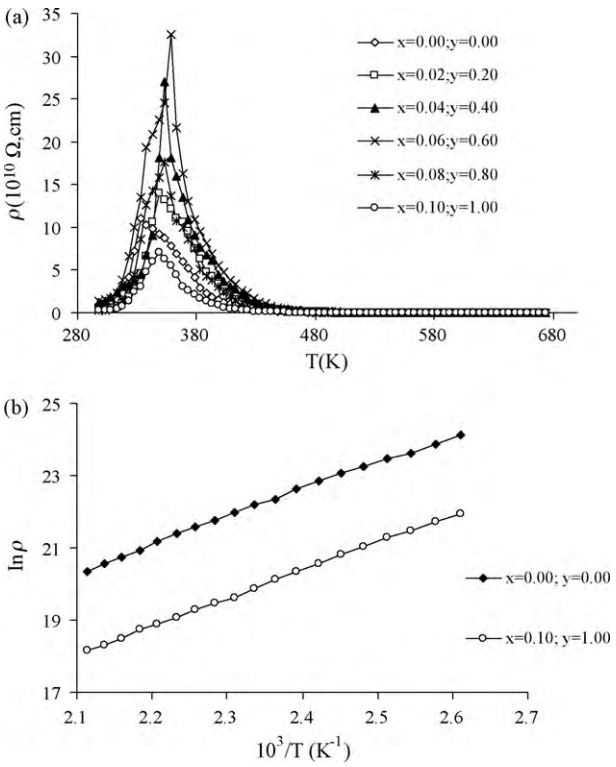

Fig. 8. (a and b) Temperature dependent DC-electrical resistivity of $Sr_{0.5}Ba_{0.5-x}Pr_xFe_{12-y}Ni_yO_{19}$ ($x = 0.00–0.100$, $y = 0.00–1.00$) samples containing different Pr–Ni contents.

The substitution of Pr^{3+} to the Ba^{2+} ions may as well induce a perturbation in both the electron-density and the symmetry around the 2b lattice site. A Pr^{3+} ion near the octahedral site could change the separation between Fe^{2+} and Fe^{3+} ions, and reduce the Fe^{2+}–O–Fe^{3+} bond angle, as well [31]. This impedes the electron-transfer between the Fe^{2+}/Fe^{3+} ions and hence increase the resistivity. It is reported that Ni^{2+} ions show a strong tendency to occupy the octahedral lattice sites ($4f_2$, 12k) [5]. Doping of the Sr–Ba hexaferrite with the Pr–Ni ions may replace some of the Fe^{3+} at the octahedral site, hence increasing the resistivity. The increase in resistivity is of significant importance from a technological point of view, as it makes these ferrites suitable for microwave devices where eddy current losses become appreciable.

An increase in the substitution level $x > 0.06$, $y > 0.60$, is associated with a fall in the values of ρ is observed (Table 1). This is interpreted in terms of two fold valence fluctuations of (i) the Pr ion between Pr^{3+} and Pr^{4+} valance states and (ii) the Ni between Ni^{2+} and Ni^{3+} that is likely to occur during the annealing process [36,37]. The exchange interactions of the type shown below may become possible:

$$Fe^{3+} + Ni^{2+} \leftrightarrow Fe^{2+} + Ni^{3+} \tag{7}$$

$$Pr^{3+} + e \leftrightarrow Pr^{4+} \tag{8}$$

The conduction due to hole-hopping between Ni^{2+}/Ni^{3+} and Pr^{3+}/Pr^{4+} ions causes the resistivity to decrease [3]. Secondly, the re-arrangement of the Fe^{3+} ions at the octahedral and tetrahedral sites may also result from the perturbation caused by doping with the Pr^{3+}. The iron ions are likely to partially migrate to the octahedral site to increase number of Fe^{3+} ions at the site leading to decrease in the resistivity. Similar findings for nanocrystalline ferrite materials have been reported elsewhere [38].

The DC-electrical resistivity of these ferrites follows Arrhenius-type temperature dependence [19]. The values of activation energy

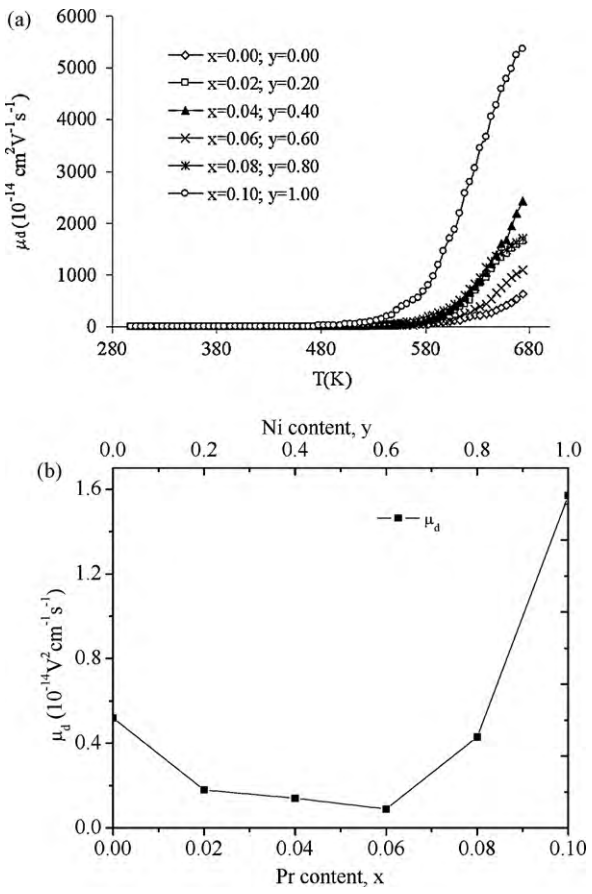

Fig. 9. (a) Plots of drift mobility (μ_d) versus temperature (T) of Sr–Ba hexaferrite samples containing different Pr–Ni content and (b) effect of Pr–Ni contents on the drift mobility (μ_d) of Sr–Ba hexaferrite samples at 423 K.

for hopping (E_a) are computed from $\ln\rho$ versus $10^3/T$ plots in the temperature range 383–483 K, shown as Fig. 8b. The value of activation energy of pure Sr–Ba hexaferrite is 0.64 eV, which increases to 0.69 eV by increasing the dopant contents up to $x = 0.06$, $y = 0.60$ (Table 1). These values are higher than the transition energy of Fe^{2+} and Fe^{3+} ($E_e = 0.2$ eV), which indicates that the small-polaron model of electron-hopping conduction mechanism is favored in the studied samples. The compositional dependence of E_a is similar to that of the resistivity (Table 1) where samples with high electrical resistivity are associated with high value of E_a. The drift mobility (μ_d) of the charge carriers is calculated from the experimental values of the DC-electrical resistivity using the following relation:

$$\mu_d = \frac{1}{ne\rho}, \tag{9}$$

where e is the charge of electron, ρ is the electrical resistivity and n is the concentration of charge carriers that can be calculated from the following equation:

$$n = \frac{N_A d_m P_{Fe}}{M}, \tag{10}$$

where N_A is Avogadro's number, M is the molecular mass of the compound, P_{Fe} is the number of iron atoms in the chemical formula of the ferrite samples and d_m is the bulk density. Fig. 9(a) shows that the drift mobility increases with the temperature. This represents the enhanced mobility of the charge carriers due to the thermal activation of the charge carriers with increasing the temperature. The magnitude of μ_d is found to be in the range of 10^{-13}–10^{-14} $cm^2\,V^{-1}\,s^{-1}$ for all the compositions. Fig. 9(b) shows that drift mobility (μ_d) calculated at 423 K decreases from 0.52×10^{-14} to 0.14×10^{-14} $cm^2\,V^{-1}\,s^{-1}$, due to the enhanced electron-hopping at the octahedral sites lending the resistivity to decrease (Table 1) as discussed above in the explanation for the DC-electrical resistivity.

4. Conclusions

XRD data of the synthesized samples point to the formation of single magnetoplumbite phase solid structures, with an average crystallite size ranging from 18 to 36 nm. The TG curve indicates that the formation of M-type hexagonal phase starts at about 1000 K. The variation in magnetic parameters is described in terms of preferential site occupancy of the substituted cations. The decrease in Curie temperature from 672 to 500 K with increasing Pr–Ni contents is interpreted in terms of the strength of exchange interactions. Temperature dependence of electrical resistivity reflects the semi-conducting nature of the ferrites. The drift mobility (μ_d) and activation energy of hopping (E_a) were calculated from the electrical resistivity data. Activation energy of hopping (E_a) was found to increase from 0.64 to 0.77 eV for the samples with $x = 0.06$, $y = 0.60$, because Pr–Ni ion substitution appears to reduce the electron exchange between the Fe^{2+} and Fe^{3+} ions at the octahedral site. The drift mobility increases with rise in temperature due to thermal activation of charge carriers. These properties are significant in terms of eddy current loss reduction in magnetic materials.

Acknowledgements

This work is supported by the Higher Education Commission (HEC) of Pakistan, under National Research Program for Universities (NRPU) scheme. The authors are thankful to Dr. Naseem Shehzad, University of the Punjab, Pakistan, for SEM analysis of our samples.

References

[1] M. Han, Y. Ou, W. Chen, L. Deng, J. Alloys Compd. 474 (2009) 185–189.
[2] H. Yanbing, J. Sha, S. Lina, T. Quan, L. Qin, J. Hongxiao, J. Dingfeng, B. Hong, G. Hongliang, X. Wang, J. Alloys Compd. 486 (2009) 348–351.
[3] M.J. Iqbal, S. Farooq, J. Alloys Compd. 493 (2010) 595–600.
[4] M.J. Iqbal, M.N. Ashiq, P.H. Gomez, J.M. Munoz, Scr. Mater. 57 (2007) 1093–1097.
[5] M.J. Iqbal, S. Farooq, Mater. Res. Bull. 44 (2009) 2050–2055.
[6] M.A. Elkestawy, J. Alloys Compd. 492 (2010) 616–620.
[7] C. Wang, X. Han, P. Xu, X. Wang, X. Li, H. Zhao, J. Alloys Compd. 476 (2009) 560–565.
[8] J. Chand, M. Singh, J. Alloys Compd. 486 (2009) 376–379.
[9] H. Su, H. Zhang, X. Tang, B. Liu, Z. Zhong, J. Alloys Compd. 475 (2009) 683–685.
[10] P. Tenaud, A. Morel, F. Kools, J.M. Le Breton, L. Lechevallier, J. Alloys Compd. 370 (2004) 331–334.
[11] L. Lechevallier, J.M.L. Breton, A. Morel, P. Tenaud, J. Phys.: Condens. Matter 20 (2008) 175203–175211.
[12] L. Lechevallier, J.M.L. Breton, J.F. Wang, I.R. Harris, J. Phys.: Condens. Matter 16 (2004) 5359–5376.
[13] G. Litsardakis, I. Manolakis, K. Efthimiadis, J. Alloys Compd. 427 (2007) 194–198.
[14] E. Melagiriyappa, H.S. Jayanna, J. Alloys Compd. 482 (2009) 147–150.
[15] H. Yamamoto, M. Isono, T. Kobayashi, J. Magn. Magn. Mater. 295 (2005) 51–56.
[16] M.N. Ashiq, S. Saleem, M.A. Malana, A. Ur-Rehman, J. Alloys Compd. 486 (2009) 640–644.
[17] Z. Yue, W. Guo, J. Zhou, Z. Gui, L. Li, J. Magn. Magn. Mater. 270 (2004) 216–233.
[18] M.J. Iqbal, M.N. Ashiq, Chem. Eng. J. 136 (2008) 383–389.
[19] M.J. Iqbal, S. Farooq, Mater. Sci. Eng. B 136 (2007) 140–147.
[20] Z. Yue, W. Guo, J. Zhou, Z. Gui, L. Li, J. Magn. Magn. Mater. 270 (2004) 216–223.
[21] M.J. Iqbal, M.N. Ashiq, P.H. Gomez, J. Alloys Compd. 478 (2009) 736–740.
[22] T.T.V. Nga, N.P. Duong, T.D. Hien, J. Alloys Compd. 475 (2009) 55–59.
[23] C. Singh, S.B. Narang, I.S. Hudiara, Y. Bai, F. Tabatabaei, Mater. Res. Bull. 43 (2008) 176–184.
[24] N. Hayashi, H. Ikuta, M. Wakihara, J. Electrochem. Soc. 146 (1999) 1351–1356.
[25] V. Dimitrov, T. Komatsu, J. Solid State Chem. 163 (2002) 100–112.
[26] T.-D.N. Phan, M.B. Song, E.J. Kim, E.W. Shin, Microporous Mesoporous Mater. 119 (2009) 290–298.
[27] L. Zhao, H. Yang, L. Yu, Y. Cui, X. Zhao, S. Feng, J. Mater. Sci. 42 (2007) 686–691.
[28] S. Ounnunkad, Solid State Comm. 138 (2006) 472–475.
[29] G.M. Suárez, L.R. Vázquez, J.C.C. Huacuz, A.F. Fuentes, J.I.E. García, Physica B 339 (2003) 110–118.

[30] L.B. Tahar, M. Artus, S. Ammar, L.S. Smiri, F. Herbst, M.J. Vaulay, V. Richard, J.M. Greneche, F. Villain, F. Fievet, J. Magn. Magn. Mater. 320 (2008) 3242–3250.
[31] M.M. El-Sayed, Ceram. Int. 33 (2007) 413–418.
[32] V. Jančárik, M. Papánová, A. Grusková, D. Kevická, J. Sláma, J. Electr. Eng. 55 (2004) 116–119.
[33] M.A. Ahmad, N. Okasha, R.M. Kershi, J. Magn. Magn. Mater. 320 (2008) 1146–1150.
[34] H.P. Pinto, S.D. Elliott, J. Phys.: Condens. Matter 18 (2006) 10427–10436.
[35] H. Kojima, in: E.P. Wolhfarth (Ed.), Handbook of Magnetic Materials, vol. 3, North-Holland Publishing, 1982, p. 368 (Chapter 5).
[36] M.A. Ahmed, N. Okasha, M.M. El-Sayed, Ceram. Inter. 33 (2007) 49–58.
[37] M.J. Iqbal, S. Farooq, Mater. Chem. Phys. 118 (2009) 308–313.
[38] M.N. Ashiq, S. Saleem, M.A. Malana, J. Alloys Compd. 486 (2009) 640–644.